Automated Model-Based Tissue Classification of MR Images of the Brain

Koen Van Leemput,* Frederik Maes, Dirk Vandermeulen, and Paul Suetens

***Abstract*—We describe a fully automated method for model-based tissue classification of magnetic resonance (MR) images of the brain. The method interleaves classification with estimation of the model parameters, improving the classification at each iteration. The algorithm is able to segment single- and multi-spectral MR images, corrects for MR signal inhomogeneities, and incorporates contextual information by means of Markov random Fields (MRF's). A digital brain atlas containing prior expectations about the spatial location of tissue classes is used to initialize the algorithm. This makes the method fully automated and therefore it provides objective and reproducible segmentations. We have validated the technique on simulated as well as on real MR images of the brain.**

***Index Terms*—Digital brain atlas, Markov random fields, MRI, segmentation, tissue classification.**

I. Introduction

THE study of many brain disorders, such as multiple sclerosis or schizophrenia, involves accurate tissue segmentation from magnetic resonance (MR) images of the brain. Manual tracing of white matter, gray matter, and cerebrospinal fluid (CSF) in MR images by a human expert is too time consuming for studies involving large amounts of data and is likely to show large intra- and interobserver variability, which deteriorates the significance of the analysis of the resulting segmentations. Automated and reliable intensity-based tissue classification, on the other hand, is complicated by the spectral overlap of MR intensities of different tissue classes and by the presence of a spatially smoothly varying intensity inhomogeneity or bias field [1]. A number of promising approaches have been presented to cope with these problems [2]–[4], but they still require some user interaction, making their results not fully objective and reproducible.

In contrast, in the companion paper [5] we describe a new approach for model-based bias correction and tissue classification in MR images of the brain that is completely automated. The method is based on an iterative expectation-maximization (EM) procedure that interleaves tissue classification with estimation of tissue-class-specific intensity models and bias field correction. Initialization of the iterative process using a digital brain atlas with *a priori* probability maps for the different tissue classes avoids all manual intervention, which makes our method an objective and reproducible tool for segmenting large amounts of data.

While in [5] we focus on the bias correction performed by the algorithm and its validation on simulated data, in this companion paper we concentrate on the tissue segmentation generated by the algorithm. In [5] tissue classification is done for each voxel independently, without taking the classification of its neighbors into account. In this paper, we extend the model of [5] to further improve the segmentation by incorporating contextual information during classification, using a Markov random field (MRF). The MRF is designed to facilitate discrimination between brain and nonbrain tissues, while preserving the detailed interfaces between the various tissue classes within the brain. We validate the approach, both on simulated data and on real images, by comparison with hand-segmented data.

This paper is organized as follows. Section II describes our method for automated tissue classification of MR images of the brain, including bias correction and estimation of the class-conditional intensity model and MRF parameters. The method is validated in Section III on simulated and real MR images and we discuss the results in Section IV. Finally, Section V summarizes the conclusions of the approach.

Manuscript received February 18, 1999; revised July 9, 1999. This work was supported by the EC-funded BIOMED-2 program under Grant BMH4-CT96-0845 (BIOMORPH), by the Research Fund KULeuven under Grant GOA/99/05 (VHS+), and by the EC-funded BIOMED-2 program under Grant BMH4-CT98-6048 (QAMRIC). The work of D. Vandermeulen was supported in part by the Fund for Scientific Research-Flanders (Belgium) (FWO-Vlaanderen) under Grant 1.5.397.97. the work of K. Van Leemput was supported in part by a grant from the Flemish Institute for the Improvement of the Scientific-Technological Research in the Industry (IWT). F. Maes is a Postdoctoral Fellow of Research for the Fund for Scientific Research-Flanders (Belgium) (FWO-Vlaanderen). The Associate Editors responsible for coordinating the review of this paper and recommending its publication were M. Viergever and W. Niessen. *Asterisk indicates corresponding author.*

*K. Van Leemput, F. Maes, D. Vandermeulen, and P. Suetens are with the group of Medical Image Computing (Radiology–ESAT/PSI), Faculties of Medicine and Engineering, University Hospital Gasthuisberg, Herestraat 49, B-3000 Leuven, Belgium.

Publisher Item Identifier S 0278-0062(99)09632-9.

II. ML Approach for Model-Based Segmentation of the Brain

For notational convenience, let the intensities in an MR image be denoted as a one-dimensional (1-D) array $y = \{y_1, y_2, \cdots, y_n\}$ where n is the number of voxels. Let the underlying segmentation be denoted as $z = \{z_1, z_2, \cdots, z_n\}$ where z_i indicates to which tissue type voxel i belongs. Assuming that there are K tissue types, $z_i = e_k$ for some $k, 1 \leq k \leq K$ where e_k is a unit vector whose kth component is one, all the other components being zero. The segmentation process can then be defined as an estimation problem where the underlying hidden segmentation z has to be estimated from the observed intensities y.

In this paper, we use a parameterized model for MR images of the brain to automate this estimation process. More specifically, the hidden segmentation z is modeled as the realization of a random process with some probability density function $f(z|\Phi_z)$ that is parameterized by the parameter set Φ_z. Furthermore, it is assumed that z has generated the observed intensities y with probability density function $f(y|z,\Phi_y)$ parameterized by Φ_y. As will be shown in the following, estimation of the segmentation z is straightforward once the model parameters $\Phi = \{\Phi_y, \Phi_z\}$ are known. However, estimation of these model parameters, in its turn, is helped by knowledge of the segmentation. Intuitively, both the segmentation and the model parameters can be estimated simultaneously by interleaving the segmentation with estimation of the model parameters.

The EM algorithm [6] formalizes this intuitive approach. It estimates the maximum likelihood (ML) parameters $\hat{\Phi}$

$$\hat{\Phi} = \arg \max_{\Phi} \log f(y|\Phi)$$

by iteratively estimating the hidden data z based on the current parameter estimation Φ and recalculating Φ that maximizes the likelihood of the so-called complete data $q = (y, z)$. More specifically, the algorithm interleaves two steps:

E Step: Find the function

$$Q(\Phi|\Phi^{(m)}) = E[\log f(q|\Phi)|y, \Phi^{(m)}].$$

M Step: Find

$$\Phi^{(m+1)} = \arg \max_{\Phi} Q(\Phi|\Phi^{(m)})$$

with m the iteration number. If during the M step, the next estimate $\Phi^{(m)}$ is chosen only to ensure $Q(\Phi^{(m+1)}|\Phi^{(m)}) > Q(\Phi^{(m)}|\Phi^{(m)})$, then the algorithm is called a generalized EM algorithm (GEM). It has been shown that the log likelihood $\log f(y|\Phi)$ is guaranteed to increase for EM and GEM algorithms [7]. Upon convergence, the segmentation is obtained as a byproduct as the estimated z.

Recently, we developed a GEM algorithm for automated bias field correction of MR images of the brain [5], [8], using a specific model where each voxel is randomly sampled from a parameterized intensity distribution. Since the segmentation algorithm that is presented in this paper is an extension of it, we briefly describe it in Section II-A. The model is then extended in Section II-B by adding a regularization component using the concept of MRF's. Section II-C explains how a digital brain atlas can be added to the method in order to make it a fully automated tool for segmenting brain tissue from MR images. We describe some implementation issues in Section II-D and we finally show how the method works on a simple example in Section II-E.

A. The Independent Model

Consider the following simple model for an MR image. The tissue type of voxel i, represented by z_i, is drawn randomly from a collection of K possible classes, each with its own known probability $P(k)$ for $1 \le k \le K$. That is

$$f(z_i = e_k) = P(k).$$

Suppose furthermore that the intensity of a voxel belonging to class k is normally distributed around a certain mean μ_k, with a variance σ_k^2 grouped in $\theta_k = \{\mu_k, \sigma_k^2\}$. Furthermore, suppose that the spatially smoothly varying intensity inhomogeneity or bias field can be written as a linear combination $\Sigma_j\ c_j\phi_j(x)$ of smoothly varying basis functions $\phi_j(x)$ with $1 \le j \le J$ where J is the number of basis functions and x denotes the spatial position. Let $C = \{c_1, c_2, \cdots, c_J\}$ denote the bias field parameters and $\Phi_y = \{\theta_1, \cdots, \theta_K, C\}$ the overall model parameters. The bias field in MR is usually modeled as a multiplicative effect. We therefore work on log-transformed intensities, which makes the bias additive. The probability density for voxel intensity y_i in voxel i, given that it belongs to class k, is then

$$f(y_i|z_i = e_k, \Phi_y) = G_{\sigma_k}\left(y_i - \mu_k - \sum_j\ c_j\phi_j(x_i)\right)$$

where $G_\sigma()$ denotes a zero-mean normal distribution with variance σ^2.

Application of the EM algorithm that searches for the ML estimation of the model parameters Φ_y yields the following equations (see Appendix A):

$$p_{ik}^{(m+1)} \equiv [p_i^{(m+1)}]_k = \frac{f(y_i|z_i = e_k, \Phi_y^{(m)}) f(z_i = e_k)}{\sum_{j=1}^{K} f(y_i|z_i = e_j, \Phi_y^{(m)}) f(z_i = e_j)} \tag{1}$$

$$\mu_k^{(m+1)} = \frac{\sum_{i=1}^{n} p_{ik}^{(m+1)} \left(y_i - \sum_{j=1}^{J} c_j^{(m)} \phi_j(x_i)\right)}{\sum_{i=1}^{n} p_{ik}^{(m+1)}} \tag{2}$$

$$(\sigma_k^{(m+1)})^2 = \frac{\sum_{i=1}^{n} p_{ik}^{(m+1)} \left(y_i - \mu_k^{(m+1)} - \sum_{j=1}^{J} c_j^{(m)} \phi_j(x_i)\right)^2}{\sum_{i=1}^{n} p_{ik}^{(m+1)}} \tag{3}$$

$$\begin{bmatrix} c_1^{(m+1)} \\ c_2^{(m+1)} \\ \vdots \end{bmatrix} = (A^t W^{(m+1)} A)^{-1} A^t W^{(m+1)} r^{(m+1)} \tag{4}$$

with

$$A = \begin{bmatrix} \phi_1(x_1) & \phi_2(x_1) & \cdots \\ \phi_1(x_2) & \phi_2(x_2) & \cdots \\ \vdots & \vdots & \ddots \end{bmatrix},$$

$$W^{(m+1)} = \mathrm{diag}(w_i^{(m+1)})$$

$$w_i^{(m+1)} = \sum_{k=1}^{K} w_{ik}^{(m+1)}$$

$$\tilde{y}_i^{(m+1)} = \frac{\sum_{k=1}^{K} w_{ik}^{(m+1)} \mu_k^{(m+1)}}{\sum_{k=1}^{K} w_{ik}^{(m+1)}}$$

$$r^{(m+1)} = \begin{bmatrix} y_1 - \tilde{y}_1^{(m+1)} \\ y_2 - \tilde{y}_2^{(m+1)} \\ \vdots \end{bmatrix},$$

$$w_{ik}^{(m+1)} = p_{ik}^{(m+1)} / (\sigma_k^{(m+1)})^2$$

where m denotes the iteration number.

These equations can be interpreted as three interleaved steps: classification of the voxels (1); estimation of the normal distributions (2) and (3); and estimation of the bias field (4). Previously, we have given a more detailed description of the algorithm and its practical use [5], [8]. Therefore, we direct the interested reader to these papers for more details. Suffice it to say that we use polynomials for the basis functions $\phi_j(x)$ and that the algorithm is easily extended to multispectral MR data by substituting the normal distributions with mean μ_k and variance σ_k^2 to multivariate normals with mean $\boldsymbol{\mu}_k$ and covariance matrix $\boldsymbol{\Sigma}_k$.

B. Regularization Using MRF's

The independent model of Section II-A classifies the voxels based on their intensity only. This yields acceptable segmentation results as long as the different classes are well separated in intensity feature space, i.e., have a clearly discernible associated intensity distribution. Unfortunately, this is not always true for MR images of the brain, especially when only one MR channel is available. Whereas such tissues as white matter, gray matter, and CSF usually have a characteristic intensity, voxels surrounding the brain often show an MR intensity that is very similar to brain tissue. This results in erroneous classifications of small regions surrounding the brain as gray matter or white matter.

We therefore extend the MR model by incorporating general spatial and anatomical constraints, such as that a voxel surrounded by nonbrain tissue cannot belong to gray matter, by introducing the concept of MRF's. The hidden data z are assumed to be a realization of a random process where the probability that voxel i belongs to tissue type k depends on the tissue type of its neighbors. The Hammersley–Clifford theorem states that such a random field is a Gibbs Random Field (see [9] and the references therein), i.e., its configurations obey a Gibbs distribution

$$f(z|\Phi_z) = Z(\Phi_z)^{-1} \exp[-U_{\mathrm{mrf}}(z|\Phi_z)]$$

where $Z(\Phi_z) = \Sigma_z \ \exp[-U_{\mathrm{mrf}}(z|\Phi_z)]$ is a normalization constant called the partition function and $U_{\mathrm{mrf}}(z|\Phi_z)$ is an energy function dependent on the MRF parameters Φ_z.

We use a simple MRF that is defined on a so-called first-order neighborhood system, i.e., only the six nearest neighbors on the three-dimensional (3-D) image lattice are used. Let $\mathcal{N}_i = \{i^n, i^s, i^w, i^e, i^t, i^b\}$ denote the neighborhood of voxel i where i^n, i^s, i^w, and i^e are its four neighbors in the plane, and i^t and i^b its two neighbors out of the plane. The voxel size in MR images is equal in the x and y direction, but usually different in the z direction. We therefore assume that the interaction between a voxel with its neighbors in the x direction is the same as that with its neighbors in the y direction, but different from that with its neighbors in the z direction. Therefore, we use the following Potts model (the $m$ary extension of the binary Ising model [10]):

$$U_{\mathrm{mrf}}(z|\Phi_z) = \sum_{i=1}^{n} U_{\mathrm{mrf}}(z_i|z_{|\mathcal{N}_i}, \Phi_z)$$

where

$$z_{\mathcal{N}_i} = \{z_{i'} | i' \in \mathcal{N}_i\}$$

stands for the set of labels at the six sites neighboring i and

$$U_{\mathrm{mrf}}(z_i|z_{\mathcal{N}_i}, \Phi_z) = z_i^t G g_i + z_i^t H h_i$$

where

$$g_i = z_{i^n} + z_{i^s} + z_{i^w} + z_{i^e}$$

is a vector that counts per class k the number of neighbors of i within the plane that belong to k. Similarly,

$$h_i = z_{i^t} + z_{i^b}$$

counts per class k the number of neighbors out of the plane that belong to k. G and H are $K \times K$ matrices that together form the MRF parameters $\Phi_z = \{G, H\}$.

With the addition of the MRF, there are now two parameter sets Φ_y and Φ_z. As explained in Appendix B, the exact calculation of Φ_y is no longer practically feasible and we use an approximation based on the so-called mean field theory, as proposed by Zhang [11] and Langan *et al.* [12]. More specifically, (2)–(4) remain valid, but the classification step is no longer given by (1) but by

$$\begin{aligned} p_{ik}^{(m+1)} &\equiv [p_i^{(m+1)}]_k \\ &\simeq \frac{f(y_i|z_i = e_k, \Phi_y^{(m)}) f(z_i = e_k|p_{\mathcal{N}_i}^{(m)}, \Phi_z^{(m)})}{\sum_{j}^{K} f(y_i|z_i = e_j, \Phi_y^{(m)}) f(z_i = e_j|p_{\mathcal{N}_i}^{(m)}, \Phi_z^{(m)})} \end{aligned} \quad (5)$$

where

$$f(z_i = e_k|p_{\mathcal{N}_i}^{(m)}, \Phi_z^{(m)}) = \frac{e^{-U_{\mathrm{mrf}}(e_k|p_{\mathcal{N}_i}^{(m)}, \Phi_z^{(m)})}}{\sum_{j=1}^{K} e^{-U_{\mathrm{mrf}}(e_j|p_{\mathcal{N}_i}^{(m)}, \Phi_z^{(m)})}}.$$

The difference lies herein, that in the independent model each voxel had the same *a priori* probability $f(z_i = e_k)$ to

belong to class k, whereas now this probability depends on the classification of the neighboring voxels.

The calculation of the MRF parameters $\Phi_z = \{G, H\}$ is more difficult. Zhang [11] used an approximation based on the same mean field idiom

$$f(z|\Phi_z^{(m)}) \simeq \prod_i \frac{e^{-U_{\mathrm{mrf}}(z_i|p_{\mathcal{N}_i}^{(m)}, \Phi_z^{(m)})}}{\sum_{z_i'} e^{-U_{\mathrm{mrf}}(z_i'|p_{\mathcal{N}_i}^{(m)}, \Phi_z^{(m)})}}. \tag{6}$$

This results in an expression that is very similar to Besag's pseudo-likelihood approach [9] for estimation of the MRF parameters Φ_z for fully labeled data z, but now with $p^{(m)}$ from (5) instead of z. Unfortunately, even with this pseudo-likelihood approximation, it is not possible to derive closed-form expressions for Φ_z as it was the case for Φ_y. Instead, numerical maximization methods for solving the nonlinear equations must be used. However, these are rather time consuming and the solution can differ depending on the initial estimate.

We therefore use a more efficient heuristic approach that is noniterative, using a least squares (LS) fit procedure [9]. Hereto, we define a $2K^2 \times 1$ vector θ that denotes all parameters G and H

$$\theta = [G_{11} \cdots G_{1K} | G_{21} \cdots G_{2K} | \cdots | G_{K1} \cdots G_{KK} | H_{11} \cdots H_{1K} | H_{21} \cdots H_{2K} | \cdots | H_{K1} \cdots H_{KK}]^t$$

and an equally sized configuration vector v_{z_i, g_i, h_i}

$$v_{z_i, g_i, h_i} = [z_{i1} g_i^t \quad z_{i2} g_i^t \quad \cdots \quad z_{iK} g_i^t | z_{i1} h_i^t \quad z_{i2} h_i^t \quad \cdots \quad z_{iK} h_i^t]^t.$$

In Appendix C, we show that for any neighborhood configuration $\{g_i, h_i\}$ and for any two distinct values z_i and z_i', the following holds:

$$[v_{z_i, g_i, h_i}^t - v_{z_i', g_i, h_i}^t]\theta = \log\left(\frac{f(z_i, g_i, h_i|\Phi_z)}{f(z_i', g_i, h_i|\Phi_z)}\right). \tag{7}$$

Each distinct combination of z_i, z_i', g_i, and h_i defines one such equation. Supposing that $f(z_i, g_i, h_i|\Phi_z)$ can somehow be estimated, one obtains an over determined linear system of equations that can be solved using a standard LS method. This would provide an estimation of the MRF parameters.

During iteration $(m+1)$ we estimate $f(z_i, g_i, h_i|\Phi_z^{(m+1)})$ by constructing a histogram $\mathcal{H}(z_i, g_i, h_i|\Phi_z^{(m+1)})$ that counts how many times a specific configuration $\{z_i, g_i, h_i\}$ occurred in the current classification $p^{(m+1)}$. Since $p^{(m+1)}$ is a soft classification, the contribution of a voxel i to the histogram entry $\mathcal{H}(z_i, g_i, h_i|\Phi_z^{(m+1)})$ is given by the probability that its configuration is $\{z_i, g_i, h_i\}$. Subsequently, $f(z_i, g_i, h_i|\Phi_z^{(m+1)})$ is estimated by $\mathcal{H}(z_i, g_i, h_i|\Phi_z^{(m+1)})/n$. Solving the linear system of (7) then provides the estimation $\Phi_z^{(m+1)}$.

To summarize, the complete EM algorithm interleaves four steps: classification of the voxels (5); estimation of the normal distribution parameters (2) and (3); estimation of the bias field (4); and estimation of the MRF parameters (7). The classification step (5) shows a remarkable similarity with the iterated conditional modes (ICM) algorithm [13]. ICM is a local optimization algorithm that tries to find the most likely hidden data z given the data y and the parameters Φ_y and Φ_z. It iteratively updates the discrete labels z by assigning the label of each voxel to

$$z_i^{(m+1)} \leftarrow \arg\max_{z_i} \frac{f(y_i|z_i, \Phi_y) f(z_i|z_{\mathcal{N}_i}^{(m)}, \Phi_z)}{\sum_{z_i'} f(y_i|z_i', \Phi_y) f(z_i'|z_{\mathcal{N}_i}^{(m)}, \Phi_z)}.$$

Comparing the above to (5), it can be seen that the EM algorithm is a soft implementation of the ICM algorithm, i.e., the classification $p^{(m+1)}$ is updated in a soft sense rather than with discrete labels. The difference with the ICM algorithm lies herein, that the parameters Φ_y and Φ_z are updated each iteration.

C. Initialization with a Digital Brain Atlas

The algorithm presented above interleaves classification, distribution parameter estimation, bias field parameter estimation, and MRF parameter estimation. We initially set the bias field parameters to zero and start the iterations by providing the algorithm with a rough prior estimation of the classification p_i in every voxel i. The distribution parameters are then estimated using (2) and (3), after which a first estimate of the bias field is made with (4) and the MRF parameters are calculated using (7). Subsequently, (5) is used to calculate a new estimate of the tissue classification, etc.

The prior classification is derived from a digital brain atlas that contains spatially varying prior probability maps for the location of white matter, gray matter, and CSF (see [5] for more details). The use of the atlas avoids interactive user intervention to initialize the algorithm, which makes the results reproducible and objective and allows the method to be fully automated.

We also use the atlas for constraining the classification process during the subsequent iterations of the algorithm, since it contains extra spatial information in case of overlapping intensities between distinct classes. More specifically, we multiply the prior probability $f(z_i = e_k|z_{\mathcal{N}_i}, \Phi_z^{(m)})$ in (5) in every voxel i by the prior probability of class k in the atlas. This also makes the algorithm more robust in case of very severe bias fields.

D. Implementation

In this section, we describe our practical approach and the implementation that was used to validate the method in Section III.

We use four classes: white matter (class 1); gray matter (class 2); CSF (class 3); and other (class 4). As explained in [5], the other class is represented by two normal distributions and one distribution that models the background noise in MR. The prior probability $f(z_i|z_{\mathcal{N}_i}, \Phi_z)$ for these classes is obtained by simply dividing the prior probability for other equally over these three distributions.

The MRF parameters G and H are 4×4 matrices. The (k, j)th element describes the contribution to the energy function $U_{\mathrm{mrf}}(z_i = e_k|z_{\mathcal{N}_i}, \Phi_z)$ of a neighboring voxel that belongs to class j. Direct application of this model favors

configurations of z where each class is spatially clustered. More specifically, a homogeneous region of white matter would preferably be surrounded by a homogeneous region of gray matter, in its turn surrounded by CSF that is finally surrounded by other. Small regions outside the brain that are misclassified as brain tissue are not preferable, and the MRF helps avoid such misclassifications.

However, it has been described in the literature that fine structures, such as the interface between white matter and gray matter, can be erased by the Potts/Ising MRF model [3], [14]. The MRF over regularizes such subtle borders and attempts to produce nicely smooth interfaces. We therefore propose a modification that penalizes impossible combinations, such as a gray matter voxel surrounded by voxels belonging to other, while at the same time preserving edges between tissues that are known to border each other. We impose that a voxel surrounded by white-matter and gray-matter voxels must have the same probability to be white matter as to be gray matter. With the class numbers defined above, this can be achieved by imposing the constraints that $G_{11} = G_{21}$ and $G_{12} = G_{22}$, the same for H. As a result, voxels surrounded by brain tissues have a low probability for CSF and other and a high, but equal, probability for white and gray matter. The actual decision between white and gray matter is therefore only based on the intensity, so that the interface between white and gray matter is unaffected by the MRF.

The same rationale applies for the interface between gray matter and CSF ($G_{22} = G_{32}$ and $G_{23} = G_{33}$, the same for H), and to the interface between CSF and other ($G_{33} = G_{43}$ and $G_{34} = G_{44}$, the same for H). This reduces the number of MRF parameters to be estimated by (7) from $2 \times 4^2 = 32$ to 20. The constraint that $G_{jk} = G_{lk}$ can easily be implemented by adding the corresponding columns in (7) before solving the linear system of equations.

The EM procedure can be iterated until either the parameter estimates converge or some maximum number of iterations is reached. The ultimate stop criterion detects when the log-likelihood $\log f(y|\Phi)$ stops increasing significantly, since this is after all the objective function that the EM algorithm maximizes. However

$$\log f(y|\Phi^{(m)}) = \log \left[\sum_z f(y|z, \Phi_y^{(m)}) f(z|\Phi_z^{(m)}) \right]$$

requires calculation of all the possible realizations of the MRF, which is computationally not feasible. We therefore once more call upon the mean field theory by approximating $f(z|\Phi_z^{(m)})$ using (6)

$$\begin{aligned} &\log f(y|\Phi^{(m)}) \\ &\quad \simeq \log \sum_z \prod_{i=1}^{n} [f(y_i|z_i, \Phi_y^{(m)}) f(z_i|p_{\mathcal{N}_i}^{(m)}, \Phi_z^{(m)})] \\ &\quad = \sum_{i=1}^{n} \log \sum_{z_i} f(y_i|z_i, \Phi_y^{(m)}) f(z_i|p_{\mathcal{N}_i}^{(m)}, \Phi_z^{(m)}). \quad (8) \end{aligned}$$

Note that evaluation of this objective function involves no additional computational burden, since the contribution of each voxel is calculated anyway during the classification step as the denominator of (5).

We have implemented the method in C language and integrated it inside the Matlab-based [15] SPM96-software package [16]. The program is able to segment multispectral MR brain images and is fully automated. As a first step, we coregister and reformat all the MR channels in case of multispectral data, using the affine registration method based on maximization of mutual information of Maes *et al.* [17]. We then spatially normalize the atlas to the study image with the same registration program. The EM algorithm described above is then used to segment the images. Voxels where the atlas indicates a zero prior probability for white matter, gray matter, or CSF are of no interest and are simply discarded. To speed up the computation, we update the parameters $\Phi^{(m+1)}$ only based on a limited subset of all voxels. Only voxels are used that lie on the subgrid of the original image grid that is closest to $4 \times 4 \times 4$ mm^3. The algorithm is stopped when the relative change of the estimation of $\log f(y|\Phi)$ between two subsequent iterations drops below 0.0001, which typically occurs after approximately 25 iterations. The overall calculation time depends on the size of the images involved. It takes less than 30 min to segment a single-channel image with dimensions $256 \times 256 \times 60$ on an SGI onyx 2.

E. Example

To clarify how the algorithm works, we here illustrate by way of an example the influence each component of the method has on the resulting segmentations. We have processed the same single-channel T1-weighted image (Siemens Vision 1.5 T, 3-D MPRAGE, 256×256 matrix, 1.25 mm slice thickness, 128 slices, FOV = 256 mm, TR = 11.4 ms, TE = 4.4 ms) a number of times, each time leaving some step out of the algorithm (see Fig. 1).

The first time, we set the order of the bias field polynomial and the MRF parameter matrices G and H to zero, which reduces the method to the application of the independent model, as described in Section II-A where the bias field estimation step is left out. The second time, G and H were again fixed to zero, but now the order of the bias field polynomial was set to four. Fig. 1(b) and (c) shows the gray-matter component of the classification probability p upon convergence for both situations. Without bias correction, white matter at the top of the brain is misclassified as gray matter, whereas the result is clearly much better when the bias correction step is added to the algorithm. However, some tissues surrounding the brain have intensities that are similar to brain tissue and are wrongly classified as gray matter.

We then added the MRF parameter estimation step and again ran the algorithm with bias polynomial order set to four. It can be seen from Fig. 1(d) that addition of the MRF results in a better distinction between brain tissues and tissues surrounding the brain. This is most beneficial in the case of single-channel MR data, where it is often difficult to discern such tissues based on their intensity only. The MRF cleans up the segmentations of brain tissues, while preserving the

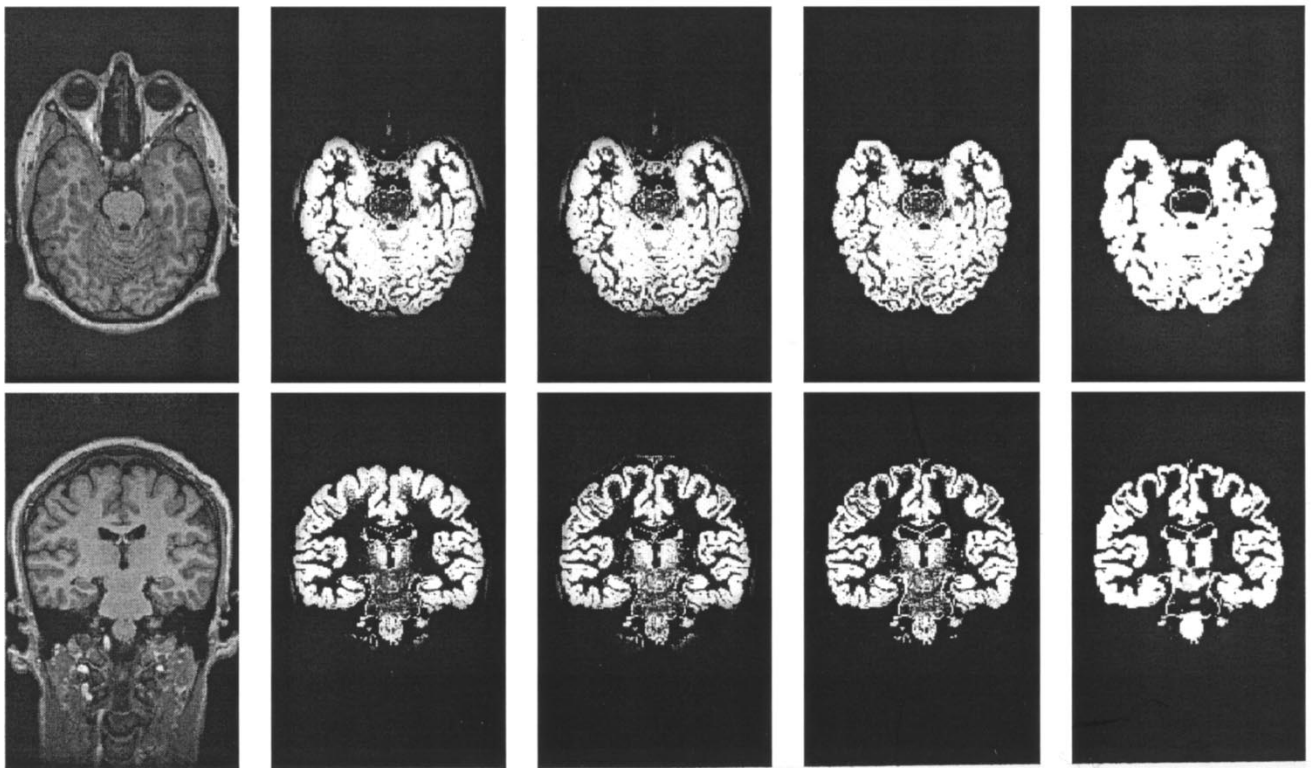

(a) (b) (c) (d) (e)

Fig. 1. Example of how the different components of the algorithm work. (a) T1-weighted image. (b) Gray-matter segmentation without bias field correction and MRF. (c) Gray-matter segmentation with bias field correction but without MRF. (d) Gray-matter segmentation with bias field correction and MRF. (e) Gray-matter segmentation with bias field correction and MRF without constraints.

detailed interface between gray and white matter and between gray matter and CSF. Fig. 2 depicts a 3-D volume rendering of the gray matter segmentation map when the MRF is used.

To demonstrate why we impose additional constraints on the interaction matrices G and H, described in Section II-D, we have processed the same image once more, but now without the constraints. We started from the previous segmentation [Fig. 1(d)], reestimated G and H from there without the constraints, and performed the classification step until convergence while keeping the parameters fixed. As can be seen from Fig. 1(e), the resulting segmentation now shows nicely distinct regions, but small details, such as small ridges of white matter, are lost. The MRF prior has over regularized the segmentation and should therefore not be used in this form. By imposing the additional constraints on G and H, we only use the MRF to penalize combinations that are not possible. This helps to clean up the segmentation maps of the brain tissues, but leaves fine details intact.

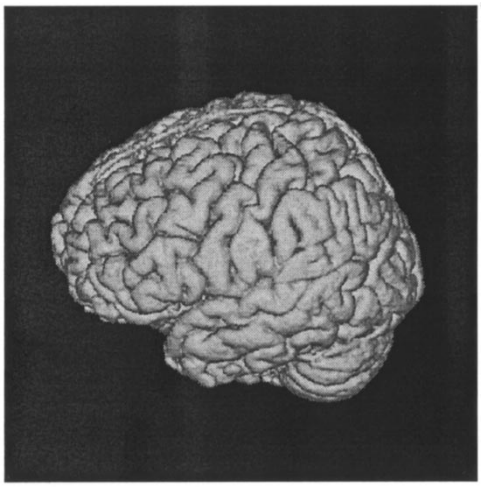

Fig. 2. 3-D volume rendering of the gray-matter segmentation of the data of Fig. 1 with bias field correction and MRF.

III. Validation

A. Simulated Data

Although the algorithm should be validated on real MR data, a comprehensive validation is easier performed on simulated images, since the ground truth is not known for *in vivo* data. Furthermore, experiments with simulated data allow studying the influence of several imaging artifacts, such as noise and MR bias fields, separately.

Therefore, we have validated the EM algorithm on simulated MR images of the head (see [5] for a visual impression of these images) that were generated by the BrainWeb MR simulator [18]–[20]. We used images with an isotropic voxel size of 1 mm and studied the influence of noise, field inhomogeneity, and contrast (T1-, T2-, or PD-weighted) by comparing the automatic segmentations with the known ground truth. For this comparison, we made a hard final segmentation from the tissue classification maps produced by the automatic algorithm

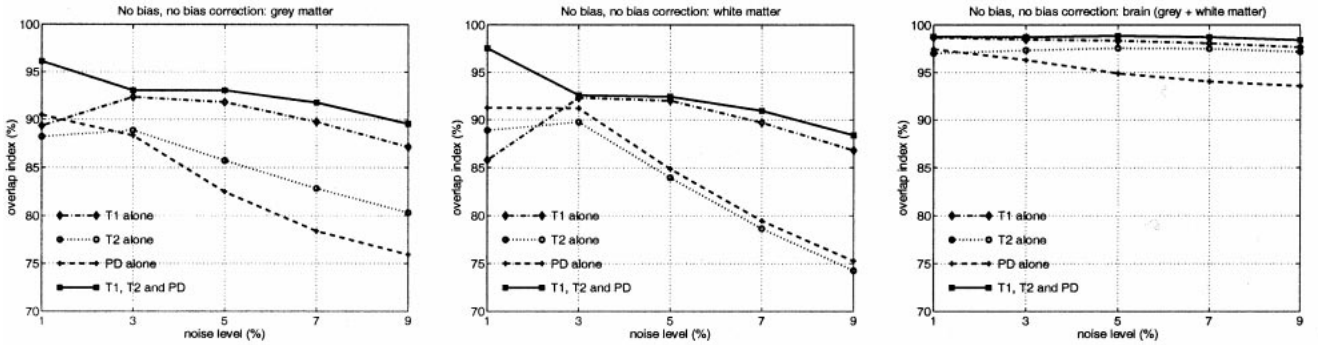

(a) (b) (c)

Fig. 3. Overlap metric between the automatic segmentation and the known ground truth for simulated MR images without bias field as a function of noise level for (a) gray matter, (b) white matter, and (c) total brain.

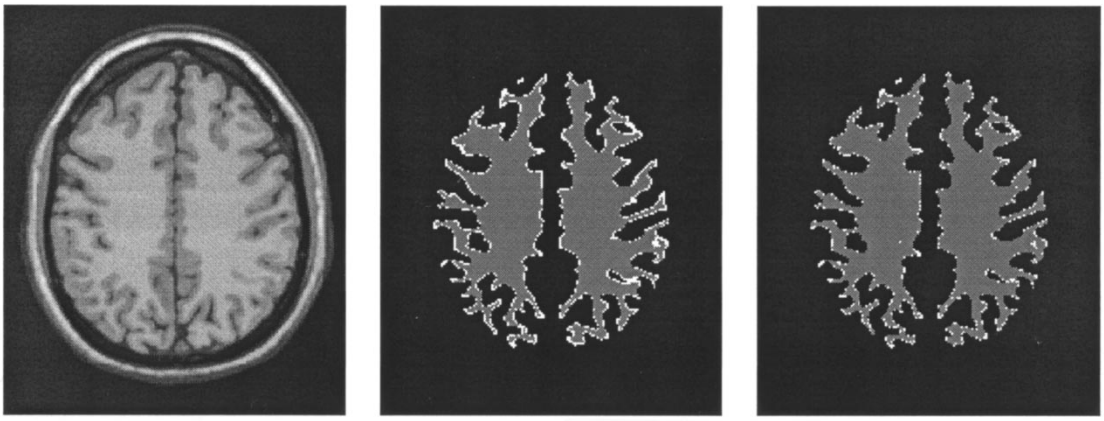

(a) (b) (c)

Fig. 4. (a) Examination of misclassified voxels on the simulated data: T1 image. (b) Misclassified white matter voxels for 1% noise. (c) Misclassified white matter voxels for 3% noise. The ground-truth white matter is shown in gray; misclassified white matter voxels are overlayed in white.

by assigning each voxel uniquely to the class where it most probably belongs. Let V_{ae}^k denote the volume of the voxels that are assigned to a class k by both the ground truth and the automatic algorithm. Similarly, let V_a^k and V_e^k denote the volume of voxels assigned to class k by, respectively, the automatic algorithm and the ground truth. We then measure the overlap between the automatic segmentation and the ground truth for class k by $2V_{ae}^k/(V_a^k + V_e^k)$. This metric, first described by Dice [21] and recently reintroduced by Zijdenbos *et al.* [22], attains the value of one if both segmentations are in full agreement and zero if there is no overlap at all.

We first investigated the influence of noise by using images that were not corrupted with a bias field. We ran the EM algorithm with the order of the bias field polynomial set to zero, i.e., no bias correction is performed, on T1-, T2-, and PD-weighted images separately and combined, for noise levels ranging from 1 to 9%. A noise level of 3% is considered typical, whereas 9% represents extreme conditions. The variation of the overlap metric for gray matter, white matter, and total brain (both together) with the noise level is depicted in Fig. 3. As a general trend, the segmentation can be seen to deteriorate with increasing noise. Furthermore, the use of all three channels (T1, T2, and PD) together yielded, in all cases, better segmentations compared to the situation where only one channel was available for the algorithm.

Surprisingly, however, the segmentation on single-channel data improves systematically when the noise level decreases from 9 to 3%, but then deteriorates again for noise level 1%. Furthermore, the total brain volume is fairly accurately segmented in all cases, whereas the segmentation of gray and white matter is generally much worse. We therefore examined the classification maps more closely and observed that both observations are caused by the same effect. Fig. 4 depicts a representative slice of the T1 data set with 1% noise and the exact location of misclassified white matter voxels in that slice for 1% and 3% noise. We concentrate on this data, since the overlap metric drop from 3 to 1% was the most remarkable for white matter segmented from T1 data in Fig. 3.

As can be seen from Fig. 4, a one-voxel-thick interface between white and gray matter is consistently misclassified in the case of 1% noise. These voxels are partial volume (PV) voxels, i.e., they have an intensity that lies somewhere in between the mean intensity of white and gray matter. Such PV voxels that do in fact not belong to either white or gray matter, but are really a mixture of both, are mostly classified to the class with the largest variance. In the absence of noise, the

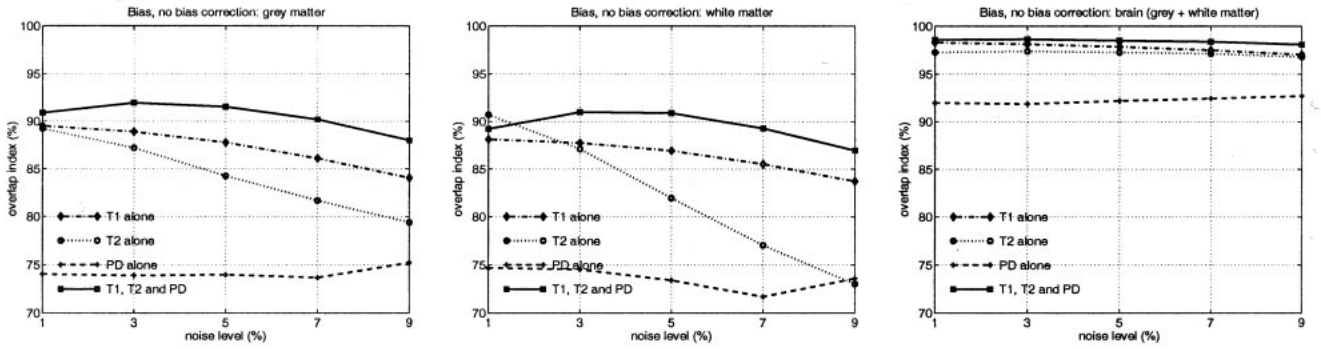

(a) (b) (c)

Fig. 5. Overlap metric between the automatic segmentation without bias correction and the known ground truth for simulated MR images with bias fields of 40% as a function of noise level for (a) gray matter, (b) white matter, and (c) total brain.

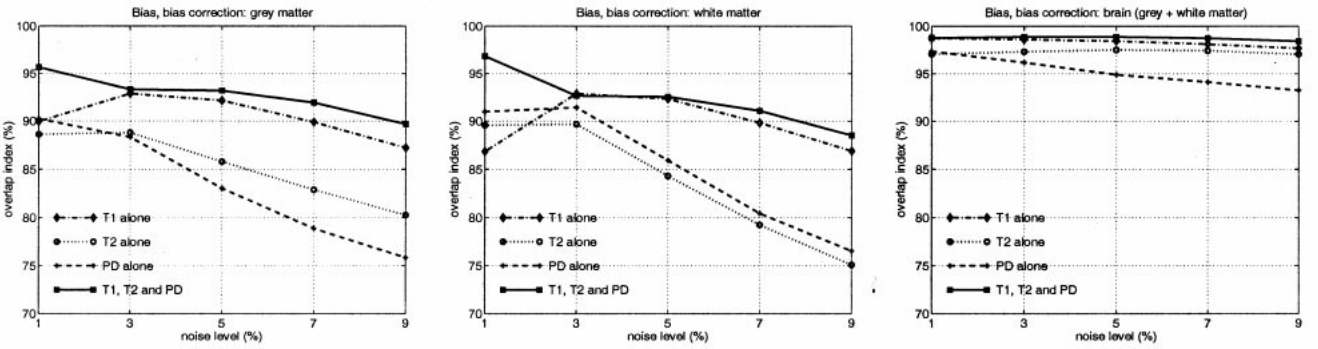

(a) (b) (c)

Fig. 6. Overlap metric between the automatic segmentation with bias field correction and the known ground truth for simulated MR images with bias fields of 40% as a function of noise level for (a) gray matter, (b) white matter, and (c) total brain.

intensity variance of pure tissue voxels around their class mean is only determined by the simulated tissue characteristics. As is the case in real MR images, gray matter shows a larger variance than white matter in the simulated data. Hence, the PV voxels are mostly classified as gray matter. When noise is introduced, the difference in variance between white and gray matter decreases, which shifts their interface slightly. Fig. 4 shows this effect clearly: when the noise level is increased from 1 to 3%, the segmentation error is reduced. Adding more noise again deteriorates the segmentation, since then pure tissue voxels start to be misclassified due to the noise.

To validate the performance of the algorithm on images that are corrupted by severe bias fields, we used simulated images with 40% field inhomogeneity. Fig. 5 depicts the segmentations when the order of the bias field polynomial was set to zero, i.e., when no bias field correction was performed. The bias field clearly deteriorates the segmentations, especially when only one channel is available to the algorithm. When, on the contrary, the order of the bias field polynomial was set to four, the segmentations were much better. This is shown in Fig. 6. Comparing these results with the ones of Fig. 3 reveals few differences, which shows that the algorithm corrects such MR field inhomogeneities well.

B. Hand-Segmented Data

We have validated the algorithm on real MR data as well, by comparing the automatic segmentations with manual tracings by a human expert. We analyzed nine datasets that were acquired on a Signa 1.5T system, having 1.17 $\times$ 1.17-mm in-plane resolution and 124 1.2-mm-thick slices acquired in the sagittal plane. These images are of the brains of children around the age of 10–16 years and were manually segmented by Robert T. Schultz, Child Study Center, Yale University, New Haven, CT. For all 124 slices, the whole brain outer surface was traced, although no attempt was made to carefully delineate all sulci. For two slices out of each dataset, one axial and one coronal, the gray–white and gray–CSF boundaries were carefully traced, trying to precisely delineate the sulci.

We compared the manual tracings with the automatic segmentations by calculating the overlap metric that was also used in Section III-A. Table I contains the result on each of the nine datasets for the total brain and for gray matter in the coronal and axial slice that was chosen for manual delineation.

By far, most of the misclassifications on the total brain are caused by the more detailed segmentation of the gray-matter–CSF interface by the automatic method compared to the manual tracing. As was the case with the simulated data, the gray matter segmentation is clearly less accurate than the total brain segmentation. Fig. 7 depicts the exact location of misclassified gray matter voxels for the coronal and axial manually traced slices of a representative dataset. It can be seen that the automatic algorithm segments the gray matter–CSF interface in more detail than the manual tracer. Some tissue surrounding the brain is still misclassified as

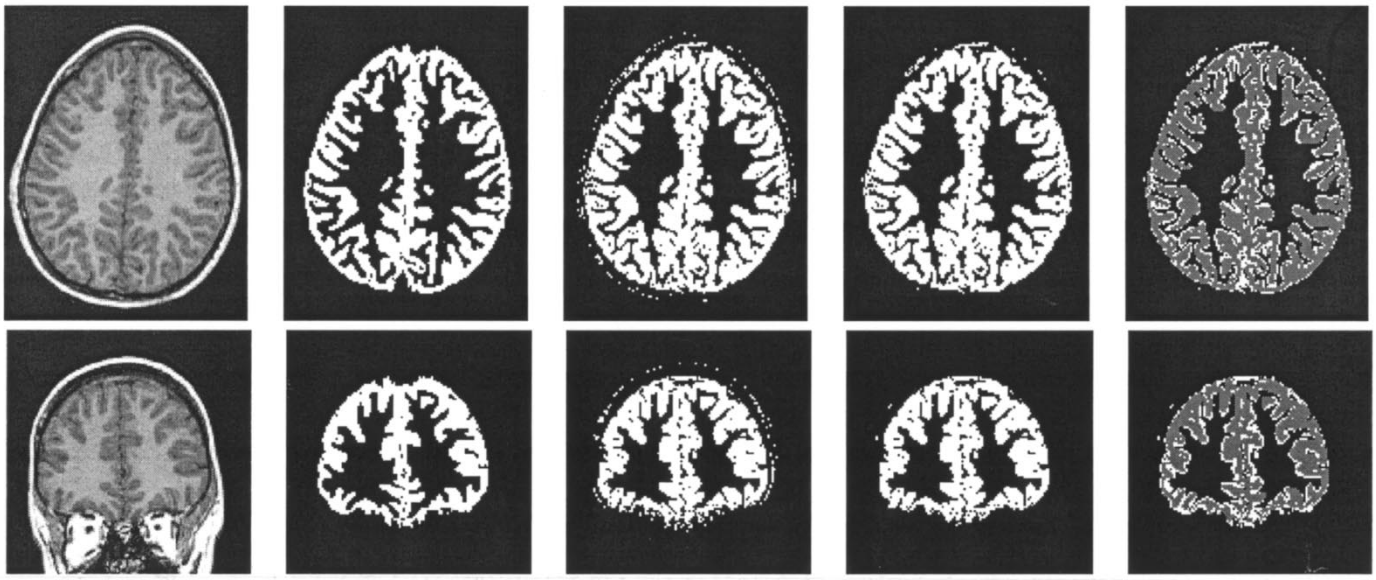

(a) (b) (c) (d) (e)

Fig. 7. Examination of voxels that are differently classified by the human tracer than by the automated method on a representative dataset. (a) Axial and coronal slice that was carefully manually segmented. (b) Corresponding manual segmentation of gray matter. (c) Automatic segmentation of gray matter without MRF prior. (d) Automatic segmentation of gray matter with MRF. (e) Difference between manual and automatic segmentation with MRF shown in white. The overlap metric is 84.4% for the axial and 83.1% for the coronal slice.

TABLE I
OVERLAP METRIC BETWEEN MANUAL AND AUTOMATIC SEGMENTATION ON NINE DATASETS OF MR IMAGES OF CHILDREN. THE TOTAL BRAIN SEGMENTATION ON THE WHOLE VOLUME WAS COMPARED, AS WELL AS GRAY MATTER SEGMENTATION OF AN AXIAL AND A CORONAL SLICE

Total brain (%)	Gray matter axial (%)	Gray matter coronal (%)
95.5	88.0	84.5
95.7	81.7	83.8
96.0	84.9	83.7
96.0	85.2	81.1
95.2	77.3	74.4
95.5	81.4	80.2
95.4	88.6	86.4
95.4	84.4	83.1
94.7	80.8	82.0

TABLE II
ESTIMATED MRF INTERACTION MATRICES FOR NINE DATASETS OF MR IMAGES OF CHILDREN (MEAN ± STANDARD DEVIATION). CLASS 1 IS WHITE MATTER, CLASS 2 GRAY MATTER, CLASS 3 CSF AND CLASS 4 OTHER

$$G = \begin{bmatrix} 0 \pm 0 & 0 \pm 0 & 2.57 \pm 0.17 & 2.96 \pm 0.07 \\ 0 \pm 0 & 0 \pm 0 & 0 \pm 0 & 1.83 \pm 0.48 \\ 3.37 \pm 0.06 & 0 \pm 0 & 0 \pm 0 & 0 \pm 0 \\ 3.03 \pm 0.08 & 2.39 \pm 0.56 & 0 \pm 0 & 0 \pm 0 \end{bmatrix}$$

$$H = \begin{bmatrix} 0 \pm 0 & 0 \pm 0 & 2.75 \pm 0.11 & 3.33 \pm 0.41 \\ 0 \pm 0 & 0 \pm 0 & 0 \pm 0 & 1.51 \pm 0.25 \\ 3.60 \pm 0.13 & 0 \pm 0 & 0 \pm 0 & 0 \pm 0 \\ 3.35 \pm 0.97 & 2.13 \pm 0.23 & 0 \pm 0 & 0 \pm 0 \end{bmatrix}$$

gray matter, although this error is already reduced compared to the situation where no MRF prior is used. However, by far most misclassifications are due to the classification of gray–white matter partial volume voxels to gray matter by the automated method. The human observer has segmented white matter consistently, as a thicker structure than the automatic algorithm.

Table II shows the final estimation of the MRF parameters G and H for these nine datasets. Since each column of both matrices is only defined up to a constant, as can be verified from (7), we normalized each column for visualization purposes by adding a constant so that the diagonal elements become zero. For each entry, we calculated the mean and the standard deviation over the nine datasets. It can be seen that the parameter estimations are fairly constant over the datasets. This should not come as a surprise, as all the images have a similar content. Because of the virtually isotropic voxelsize, the out-plane interactions H are very similar to the in-plane interactions G. Finally, the relatively high values associated with noncompatible tissue types reflect the high spatial resolution of the images. White matter is always surrounded by gray matter, which, in its turn, is consistently surrounded by CSF, which is finally surrounded by other.

IV. DISCUSSION

We have described and validated a fully automated model-based method for segmenting brain tissues from MR images. The algorithm iteratively interleaves voxel classification, intensity distribution parameter estimation, MR bias field correction, and MRF parameter estimation.

Due to the fact that the in-plane resolution is generally different than the out-plane resolution in MR images, we have modeled in-plane class transition probabilities with different parameters G than between-slice class transition probabilities parameterized by H. Since the resolution of MR images can largely vary, we reestimate G and H for every image sepa-

rately. It should be noted, however, that the MRF parameter estimation step is responsible for almost half of the total computational burden. To speed up the algorithm, one could neglect the out-plane interactions H and precalculate the in-plane interactions G just once on a normal brain dataset. Since the in-plane resolution in MR is fairly constant, this precalculated G could then be used for the segmentation of all following datasets. However, this approach does not make use of the full 3-D nature of the MR images and can therefore be expected to yield less powerful discrimination between brain and nonbrain tissues. On the contrary, if a large set of similar images with equal voxel sizes has to be segmented, both G and H could be precalculated on one image and applied to all other images of the set. Although we have not validated this approach, we expect this to speed up the process without loss of accuracy.

Application of the genuine Ising model or its $m$ary extension, the Potts model, leads to the loss of small details in the resulting segmentations, as shown in Fig. 1(e). This over regularization is a well-known effect which other models try to overcome. In particular, the so-called Chien model, first proposed by Descombes *et al.* [14], seems better adapted to medical images since it better preserves fine structures and linear shapes. Unfortunately, generalizing this two-dimensional (2-D) model to 3-D induces neighborhoods of 124 voxels and leads in practice to intractable computations [23]. A more efficient extension to 3-D has been proposed in [23], but this still involves 60 neighbors. Instead, we have imposed additional constraints on the interaction matrices G and H of the Potts model. This leads to an algorithm that is computationally efficient, involving only six neighbors, while leaving fine details intact.

A problem that showed up during the validation for both simulated and real MR data, was the PV effect. Whereas the model we used assumes that each voxel in the image belongs to only one single class, voxels that lie on the border between different tissue types violate this assumption. In reality, these voxels are a mixture of tissues and every segmentation method that tries to assign them exclusively to one class is condemned to fail. The problem is especially important in images of the brain since the interface between gray and white matter is highly complex, which results in a high volume of PV voxels compared to the volume of pure tissue voxels. Misclassification of this thin interface therefore gives immediate rise to considerable segmentation errors [24].

Ideally, the model should be adjusted to model a mixture of tissue types in each voxel rather than a single tissue type only. In the literature, a number of attempts have been made in this direction. Choi *et al.* [25] introduced the concept of so-called *mixels*, but they had to introduce heuristics in order to arrive at a workable solution. More recently, Laidlaw *et al.* [26] have applied the intensity distribution of partial volume mixtures of two tissues derived by Santago and Gage [27] to the segmentation problem. However, the time figures they sketch are still too high for the method to be practically useful. Further research is therefore needed in this direction.

Often one is not only interested in segmentations of the total white and gray matter, but also in anatomical substructures of the brain. Examples include the separation of the left and right hemisphere in the study of brain asymmetry associated with schizophrenia. While the segmentation of such anatomically defined structures is typically performed by matching a labeled atlas to the study image, using a nonrigid registration technique, these methods have difficulty in segmenting such highly variable structures as the white–gray matter interface. We are currently investigating the use of Thirion's demons [28] technique to subdivide the segmentation maps generated by the EM algorithm described above into anatomical substructures [29].

Although the MRF in combination with the digital atlas helps avoid misclassifications, it is not always sufficient to totally prevent nonbrain tissues to be misclassified as gray or white matter, as can be seen on Fig. 7. Usually, this kind of problem is addressed by mathematical morphological operations in a postprocessing step. Alternatively, deformable topological models have been proposed [30]. In a similar vein, we plan to use a nonrigid registration method to generate a new atlas by averaging the segmentations of a number of normal subjects after nonrigid matching. Compared to the atlas that we use at this moment, which was generated by averaging segmentations after affine normalization, the new a priori maps for gray matter, white matter, and CSF would be much sharper. We expect this to lead to a better fitted brain mask and, as a result, to improved segmentations.

We demonstrated the validity of the approach on simulated data and by comparison with manual segmentations by a single observer. More validation is needed to fully characterize the performance of the algorithm against a range of multiple expert segmentations. Further work includes adapting the algorithm so that it can be applied to fully automated segmentation of Multiple Sclerosis (MS) lesions in the brain for analyzing the time evolution of MS lesions during drug treatment [31].

V. Conclusions

We have presented a fully automated model-based method for tissue classification of MR images of the brain. The algorithm interleaves classification with MR bias field correction, intensity distribution estimation, and estimation of MRF parameters. We use a digital brain atlas, containing information about the expected *a priori* location of tissue types, to initialize the algorithm. This yields a fully automated method for tissue classification that produces objective and reproducible results. The method was validated on simulated and real MR images of the brain. The use of MRF's helps in discriminating between brain and nonbrain tissues. Future work will focus on the construction of a more accurate brain atlas using a nonrigid registration technique and on the investigation of the partial volume effect.

Appendix A

We here derive the EM algorithm for the independent model of Section II-A. The log likelihood for the complete data

$q = (y, z)$ can be written as

$$\begin{aligned}\log f(q|\Phi_y) &= \log f(y, z|\Phi_y) \\ &= \log f(y|z, \Phi_y) + \log f(z) \\ &= \sum_{i=1}^{n} \log f(y_i|z_i, \Phi_y) + \sum_{i=1}^{n} \log f(z_i).\end{aligned}$$

Since z_i is a vector with all zero components except for a single component that is unity, we have

$$\log f(y_i|z_i, \Phi_y) = z_i^t U(y_i|\Phi_y)$$

and

$$\log f(z_i) = z_i^t V$$

where $U(y_i|\Phi_y)$ is a vector that has as kth component $\log f(y_i|z_i = e_k, \Phi_y)$ and similar V has a kth component $\log f(z_i = e_k)$. Therefore, we have

$$\begin{aligned}Q(\Phi_y|\Phi_y^{(m)}) &= E[\log f(q|\Phi_y)|y, \Phi_y^{(m)}] \\ &= \sum_{i=1}^{n} E[z_i^t|y, \Phi_y^{(m)}] U(y_i|\Phi_y) \\ &\quad + \sum_{i=1}^{n} E[z_i^t|y, \Phi_y^{(m)}] V.\end{aligned}$$

Define $p_i^{(m+1)} \equiv E[z_i|y_i, \Phi_y^{(m)}]$ as the estimation of the hidden data z_i in voxel i based on its intensity y_i and the current parameter estimate $\Phi_y^{(m)}$. It can then be seen that

$$[p_i^{(m+1)}]_k = f(z_i = e_k|y_i, \Phi_i^{(m)})$$

which results in (1) after application of Bayes' rule. Explicit maximization of $Q(\Phi_y|\Phi_y^{(m)})$ to Φ_y yields (2) and (3) for the distribution parameters $\mu_k^{(m+1)}$ and $\sigma_k^{(m+1)}$ and (4) for the bias field parameters $c_j^{(m+1)}$ [5], [8].

APPENDIX B

We here derive the equations for the parameters Φ_y when the MRF is added. There are now two parameter sets Φ_y and Φ_z. Denoting $\Phi = \{\Phi_y, \Phi_z\}$, the log likelihood for the complete data $q = (y, z)$ now becomes

$$\log f(q|\Phi) = \sum_{i=1}^{n} \log f(y_i|z_i, \Phi_y) - U_{\text{mrf}}(z|\Phi_z) - \log Z(\Phi_z)$$

and hence

$$\begin{aligned}Q(\Phi|\Phi^{(m)}) &= \sum_{i=1}^{n} E[z_i^t|y, \Phi^{(m)}] U(y_i|\Phi_y) \\ &\quad - E[U_{\text{mrf}}(z|\Phi_z) + \log Z(\Phi_z)|y, \Phi^{(m)}].\end{aligned}$$

The parameters Φ_y can now be calculated in the same way as the independent model. However, $p_i^{(m+1)} = E[z_i|y, \Phi^{(m)}]$ can no longer been calculated with (1) since the z_i are not independent and, as a result, it is difficult to obtain the exact solution. By definition

$$\begin{aligned}E[z_i|y, \Phi^{(m)}] &= \sum_z z_i f(z|y, \Phi^{(m)}) \\ &= \frac{\sum_z z_i f(y|z, \Phi_y^{(m)}) f(z|\Phi_z^{(m)})}{f(y|\Phi^{(m)})}.\end{aligned}$$

However, due to the interaction between the z_i's, the above would involve calculation of all the possible realizations of the MRF. Therefore, exact calculation of $p_i^{(m+1)}$ is not computationally feasible and an approximate technique must be used.

We here adopt an approximation that was proposed by Zhang [11] and Langan *et al.* [12], based on the mean field theory from statistical mechanics. This mean field approach suggests an approximation to $p_i^{(m+1)}$ based on the assumption that the influence of $z_j, j \neq i$ in the calculation of $p_i^{(m+1)}$ can be approximated by the influence of $p_j^{(m)}$ from the previous iteration. This explains (5). Once $p^{(m+1)}$ is known, the equations for the parameters $\Phi_y^{(m+1)}$ can be derived in exactly the same way as with the independent model and, therefore, (2)–(4) remain valid.

APPENDIX C

We show how (7) can be obtained. Using θ and v_{z_i,g_i,h_i} as defined in Section II-B, the following holds:

$$\begin{aligned}U_{\text{mrf}}(z_i|z_{\mathcal{N}_i}, \Phi_z) &= z_i^t G g_i + z_i^t H h_i \\ &= v_{z_i,g_i,h_i}^t \theta.\end{aligned} \tag{9}$$

The conditional likelihood $f(z_i|z_{\mathcal{N}_i}, \Phi_z)$ is related to the potential $U_{\text{mrf}}(z_i|z_{\mathcal{N}_i}, \Phi_z)$ by

$$f(z_i|z_{\mathcal{N}_i}, \Phi_z) = \frac{e^{-U_{\text{mrf}}(z_i|z_{\mathcal{N}_i}, \Phi_z)}}{\sum_{z_i'} e^{-U_{\text{mrf}}(z_i'|z_{\mathcal{N}_i}, \Phi_z)}}.$$

Furthermore

$$f(z_i|z_{\mathcal{N}_i}, \Phi_z) = f(z_i|g_i, h_i, \Phi_z) = \frac{f(z_i, g_i, h_i|\Phi_z)}{f(g_i, h_i, |\Phi_z)}$$

so that

$$\frac{e^{-U_{\text{mrf}}(z_i|z_{\mathcal{N}_i}, \Phi_z)}}{f(z_i, g_i, h_i|\Phi_z)} = \frac{\sum_{z_i'} e^{-U_{\text{mrf}}(z_i'|z_{\mathcal{N}_i}, \Phi_z)}}{f(g_i, h_i|\Phi_z)}.$$

Since the right-hand side of the above is independent of the value of z_i, so is the left-hand side and therefore

$$\frac{e^{-U_{\text{mrf}}(z_i|z_{\mathcal{N}_i}, \Phi_z)}}{f(z_i, g_i, h_i|\Phi_z)} = \frac{e^{-U_{\text{mrf}}(z_i'|z_{\mathcal{N}_i}, \Phi_z)}}{f(z_i', g_i, h_i|\Phi_z)}$$

for any two distinct values z_i and z_i' .Rearranging the above and using (9), we obtain (7).

ACKNOWLEDGMENT

The authors would like to thank R. T. Schultz and J. S. Duncan from Yale University for kindly providing the hand-segmented data, and wish to acknowledge the contribution of X. Zeng.

REFERENCES

[1] J. G. Sled and G. B. Pike, "Understanding intensity nonuniformity in MRI," in *Proc. Medical Image Computing Computer-Assisted Intervention—MICCAI'98* (Lecture Notes in Computer Science). Berlin, Germany: Springer-Verlag, 1998, vol. 1496, pp. 614–622.

[2] W. M. Wells, III, W. E. L. Grimson, R. Kikinis, and F. A. Jolesz, "Adaptive segmentation of MRI data," *IEEE Trans. Med. Imag.*, vol. 15, pp. 429–442, Aug. 1996.

[3] K. Held, E. R. Kops, B. J. Krause, W. M. Wells III, R. Kikinis, and H. W. Müller-Gärtner, "Markov random field segmentation of brain MR images," *IEEE Trans. Med. Imag.*, vol. 16, pp. 878–886, Dec. 1997.

[4] T. Kapur, W. E. L. Grimson, R. Kikinis, and W. M. Wells, "Enhanced spatial priors for segmentation of magnetic resonance imaging," in *Proc. Medical Image Computing Computer-Assisted Intervention—MICCAI'98* (Lecture Notes in Computer Science). Berlin, Germany: Springer-Verlag, 1998, vol. 1496 pp. 457–468.

[5] K. Van Leemput, F. Maes, D. Vandermeulen, and P. Suetens, "Automated model-based bias field correction of MR images of the brain," *IEEE Trans. Med. Imag.*, (*Special Issue on Model-Based Analysis of Medical Images)*, vol. 18, pp. 885–896, Oct. 1999.

[6] A. P. Dempster, N. M. Laird, and D. B. Rubin, "Maximum likelihood from incomplete data via the EM algorithm," *J. R. Stat. Soc.*, vol 39, pp. 1–38, 1977.

[7] C. F. J. Wu, "On the convergence properties of the EM algorithm," *Ann. Stat.*, vol. 11, no. 1, pp. 95–103, 1983.

[8] K. Van Leemput, F. Maes, D. Vandermeulen, and P. Suetens, "Automatic segmentation of brain tissues and MR bias field correction using a digital brain atlas," in *Proc. Medical Image Computing Computer-Assisted Intervention—MICCAI'98* (Lecture Notes in Computer Science). Berlin, Germany: Springer-Verlag, 1998, vol. 1496 pp. 1222–1229.

[9] S. Z. Li, *Markov Random Field Modeling in Computer Vision* (Computer Science Workbench). Berlin, Germany: Springer-Verlag, 1995.

[10] E. Ising, "Beitrag zur Theorie des Ferromagnetismus," *Zeitschrift für Physik*, vol. 31, pp. 253–258, 1925.

[11] J. Zhang, "The mean-field theory in EM procedures for markov random fields," *IEEE Trans. Signal Processing*, vol. 40, pp. 2570–2583, Oct. 1992.

[12] D. A. Langan, K. J. Molnar, J. W. Modestino, and J. Zhang, "Use of the mean-field approximation in an EM-based approach to unsupervised stochastic model-based image segmentation," in *Proc. ICASSP'92*, San Francisco, CA, Mar. 1992, vol. 3, pp. 57–60.

[13] J. Besag, "On the statistical analysis of dirty pictures," *J. R. Stat. Soc. B*, vol. 48, no. 3, pp. 259–302, 1986.

[14] X. Descombes, J.-F. Mangin, E. Pechersky, and M. Sigelle, "Fine structure preserving markov model for image processing," in *Proc. 9th Scandinavian Conf. Image Analysis—SCIA 95*, 1995, pp. 349–356.

[15] *Matlab*. Natick MA: The MathWorks.

[16] J. Ashburner, K. Friston, A. Holmes, and J.-B. Poline, *Statistical Parametric Mapping*, The Wellcome Dept. Cognitive Neurology, Univ. College London, London, U.K. Available: http://www.fil.ion.ucl.ac.uk/spm/

[17] F. Maes, A. Collignon, D. Vandermeulen, G. Marchal, and P. Suetens, "Multi-modality image registration by maximization of mutual information," *IEEE Trans. Med. Imag.*, vol. 16, pp. 187–198, Apr. 1997.

[18] C. A. Cocosco, V. Kollokian, R. K.-S. Kwan, and A. C. Evans, "BrainWeb: Online interface to a 3D MRI simulated brain database," *NeuroImage*, vol. 5, no. 4 pt. 2/4 S425, 1997. Available:http://www.bic.mni.mcgill.ca/brainweb/

[19] R. K.-S. Kwan, A. C. Evans, and G. B. Pike, "An extensible MRI simulator for post-processing evaluation," in *Proc. Visualization in Biomedical Computing—VBC'96* (Lecture Notes in Computer Science). Berlin, Germany: Springer-Verlag, 1996, vol. 1131 pp. 135–140.

[20] D. L. Collins, A. P. Zijdenbos, V. Kollokian, J. G. Sled, N. J. Kabani, C. J. Holmes, and A. C. Evans, "Design and construction of a realistic digital brain phantom," *IEEE Trans. Med. Imag.*, vol. 17, pp. 463–468, June 1998.

[21] L. R. Dice, "Measures of the amount of ecologic association between species," *Ecology*, vol. 26, no. 3, pp. 297–302, 1945.

[22] A. Zijdenbos, B. M. Dawant, R. A. Margolin, and A. C. Palmer, "Morphometric analysis of white matter lesions in MR images: Method and validation," *IEEE Trans. Med. Imag.*, vol. 13, pp. 716–724, Dec. 1994.

[23] D. Vandermeulen, X. Descombes, P. Suetens, and G. Marchal, "Unsupervised regularized classification of multi-spectral MRI," Katholieke Universiteit Leuven, Belgium, Tech. Rep. KUL/ESAT/MI2/9608, Feb. 1996.

[24] W. J. Niessen, K. L. Vincken, J. Weickert, B. M. ter Haar Romeny, and M. A. Viergever, "Multiscale segmentation of three-dimensional MR brain images," *Int. J. Comp. Vision*, vol. 31, nos. 2/3, pp. 185–202, 1999.

[25] H. S. Choi, D. R. Haynor, and Y. Kim, "Partial volume tissue classification of multichannel magnetic resonance images—A mixel model," *IEEE Trans. Med. Imag.*, vol. 10, pp. 395–407, Sept. 1991.

[26] D. H. Laidlaw, K. W. Fleischer, and A. H. Barr, "Partial-volume bayesian classification of material mixtures in MR volume data using voxel histograms," *IEEE Trans. Med. Imag.*, vol. 17, pp. 74–86, Feb. 1998.

[27] P. Santago and H. D. Gage, "Statistical models of partial volume effect," *IEEE Trans. Image Processing*, vol. 4, pp. 1531–1540, Nov. 1995.

[28] J.-P. Thirion, "Non-rigid matching using demons," in *Proc. Computer Vision Pattern Recognition, CVPR'96*, June 1996.

[29] F. Maes, K. Van Leemput, L. E. DeLisi, D. Vandermeulen, and P. Suetens, "Quantification of cerebral grey and white matter asymmetry from MRI," in *Proc. Medical Image Computing Computer-Assisted Intervention—MICCAI'99* (Lecture Notes in Computer Science). Berlin, Germany: Springer-Verlag, 1999, vol. 1679, pp. 348–357.

[30] J.-F. Mangin, F. Tupin, V. Frouin, I. Bloch, R. Rougetet, J. Régis, and J. López-Krahe, "Deformable topological models for segmentation of 3D medical images," in *Proc. 14th Int. Conf. Information Processing Medical Imaging—IPMI 95*. Amsterdam, The Netherlands: Kluwer, 1995, pp. 153–164.

[31] K. Van Leemput, F. Maes, F. Bello, D. Vandermeulen, A. Colchester, and P. Suetens, "Automated segmentation of MS lesions from multichannel MR images," in *Proc. Medical Image Computing Computer-Assisted Intervention—MICCAI'99* (Lecture Notes in Computer Science). Berlin, Germany: Springer-Verlag, 1999, vol. 1679, pp. 11–21.